RESEARCH ARTICLE

Key Points:
- Operation IceBridge data sets used for gravity inversions in Greenland fjords
- New bathymetry in 54 fjords, new sub ice topography in outlet glaciers
- Models show fjord morphology, changes in geology, and resolve ambiguous radar

Resolving bathymetry from airborne gravity along Greenland fjords

Alexandra Boghosian[1], Kirsty Tinto[1], James R. Cochran[1], David Porter[1], Stefan Elieff[2], Bethany L. Burton[3], and Robin E. Bell[1]

[1]Lamont-Doherty Earth Observatory, Columbia University, Palisades, New York, USA, [2]Sander Geophysics Ltd., Ottawa, Ontario, Canada, [3]U.S. Geological Survey, Crustal Geophysics, and Geochemistry Science Center Box, Denver, Colorado, USA

Abstract Recent glacier mass loss in Greenland has been attributed to encroaching warming waters, but knowledge of fjord bathymetry is required to investigate this mechanism. The bathymetry in many Greenland fjords is unmapped and difficult to measure. From 2010 to 2012, National Aeronautics and Space Administration's Operation IceBridge collected a unique set of airborne gravity, magnetic, radar, and lidar data along the major outlet glaciers and fjords in Greenland. We applied a consistent technique using the IceBridge gravity data to create 90 bathymetric profiles along 54 Greenland fjords. We also used this technique to recover subice topography where warm or crevassed ice prevents the radar system from imaging the bed. Here we discuss our methodology, basic assumptions and error analysis. We present the new bathymetry data and discuss observations in six major regions of Greenland covered by IceBridge. The gravity models provide a total of 1950 line kilometers of bathymetry, 875 line kilometers of subice topography, and 12 new grounding line depths.

1. Introduction

The Greenland Ice Sheet is losing mass through both increased surface melt and ice flux into the surrounding oceans [*Shepherd et al.*, 2012]. The increased ice flux through marine-terminating glaciers [*Rignot and Kanagaratnam*, 2006] is significant and highly variable, both spatially and temporally [*Moon et al.*, 2012]. This increase in ice flux has been attributed to increased surface melting causing basal lubrication of the ice sheet [e.g., *Bartholomew et al.*, 2012; *Doyle et al.*, 2014; *Joughin et al.*, 2008; *Meirbachtol et al.*, 2013; *Zwally et al.*, 2002]. It has also been suggested that the increased ice flux is due to the encroachment of warming ocean water into fjords toward the terminus of marine-terminating glaciers resulting in increased calving and grounding line retreat which will reduce buttressing causing faster glacier flow [e.g., *Holland et al.*, 2008; *Rignot et al.*, 2012; *Seale et al.*, 2011].

In the Arctic, cold fresh polar water is layered on top of deeper warmer Atlantic water. The temperature of this deeper water below ~100 m depth ranges from 0.5°C to over 4°C in southern Greenland [*Myers and Ribergaard*, 2013; *Straneo et al.*, 2012], several degrees above the melting point of ice. While this relatively warm water has the potential to melt marine-terminating glaciers, water circulation in a fjord is controlled to first order by the fjord's geometry, including its width, depth, and presence or absence of shallow bathymetric sills [e.g., *Stygebrandt*, 2012]. The fjord bathymetry controls the warm water's path toward the glacial ice [*Gladish et al.*, 2015] through deep pathways for ocean water to advance up the fjord to the ice front.

Difficulty in conducting ship-based surveys in the ice-covered Greenland fjords has led to a dearth of fjord bathymetry data. The lack of bathymetry data in many Greenland fjords hampers our understanding of the role the warming oceans play in the increasing ice flux from marine-terminating glaciers and of ice-ocean interactions in general. Developing new bathymetric models for Greenland fjords can advance our understanding of the role that ocean forcing plays in the melting of the Greenland ice sheet.

Operation IceBridge (OIB) is a National Aeronautics and Space Administration (NASA) mission designed to bridge the gap between the ICESat I and ICESat II altimetry missions by monitoring the changing elevation of the ice sheets utilizing aircraft measurements. The IceBridge mission simultaneously acquires visual imagery, lidar altimetry, radar, gravity, and magnetic measurements in otherwise data-poor areas to comprehensively measure the entire ice sheet and surrounding polar oceans. IceBridge flights in Greenland collected gravity data from 2010 to 2012 (Figure 1). These flights include 211 lines along glacier and fjord centerlines.
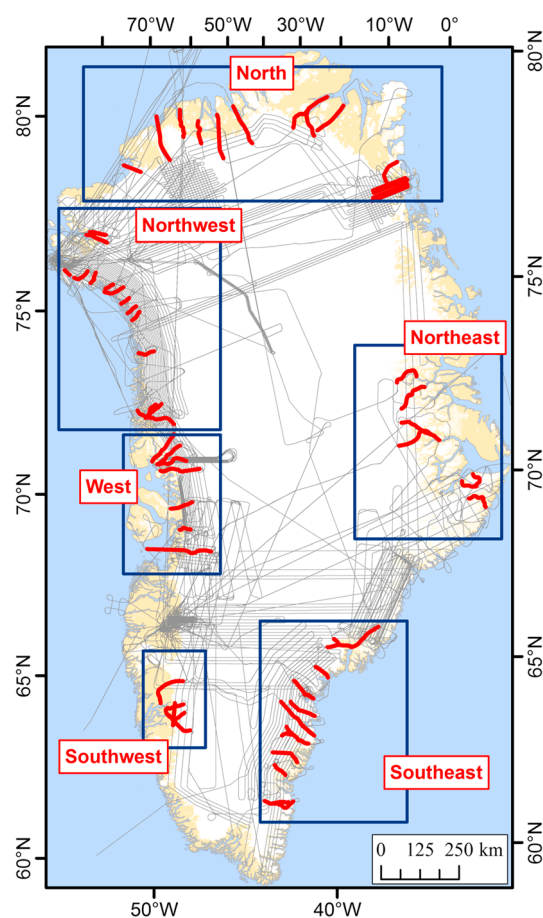
Figure 1. Location of low-elevation Operation IceBridge (OIB) flight lines from 2010 to 2012 (black). The red lines show the 54 fjords where gravity data was used to produce new bathymetry in the fjord and/or new topography beneath the ice sheet. The blue boxes mark regions described in the supporting information.

Much of the global bathymetry widely used by the science community is a gravity-based bathymetric model. The gravity field derived from satellite altimetry observations of the sea surface has been used to model ocean bathymetry since the Seasat mission in the 1980s [*Haxby et al.*, 1983] and forms the basis of bathymetry maps of the global oceans [e.g., *Sandwell et al.*, 2014; *Smith and Sandwell*, 1997]. The IceBridge gravity data, together with the other data sets, provide a powerful basis for building new bathymetry and subice topography models in data-poor regions. While radar is the primary tool for imaging subice topography, radar cannot recover water depth in fjords or under floating ice. Radar also often cannot recover ice thickness measurements from the ice sheet bed in the warm, heavily crevassed ice of outlet glaciers such as those of southern Greenland. IceBridge gravity data can provide estimates of subglacial topography in areas where the radar system cannot, as well as provide grounding line depths of glaciers, and bathymetry in the fjords. Gravity-based models can smoothly fill in the data gap between onshore subice topography from radar and offshore bathymetry measurements from shipborne surveys (Figure 2).

Gravity modeling of fjord bathymetry using IceBridge data has been used to investigate the bathymetry of Petermann fjord [*Tinto et al.*, 2015] and to analyze the relationship between grounding line depths and mass wastage in a pair of glaciers (Tracy Gletscher and Heilprin Gletscher) in northwest Greenland [*Porter et al.*, 2014]. This method has also been used to recover bathymetry under the Larsen, Abbot, Pine Island, and Thwaites Ice Shelves in Antarctica [*Cochran and Bell*, 2012; *Cochran et al.*, 2014; *Muto et al.*, 2013; *Tinto and Bell*, 2011].

The gravity-derived bathymetry that we present here is the first comprehensive effort to provide subice topography in heavily crevassed regions and under warm ice, as well as fjord bathymetry and grounding line depths throughout Greenland. We use along-fjord-axis IceBridge survey lines to create 2-D bathymetry profiles along 54 distinct Greenland fjords (Figure 1). Here we detail the instruments used, the inversion methodology employed, and present a detailed error analysis of the approach. We present new fjord bathymetry for six distinct regions in Greenland. We highlight specific examples in the data set that illustrate the use of offshore bathymetric constraints, coincident and intersecting flights, and the use of IceBridge magnetic data in model evaluation. We also compare the new gravity-derived models to other bed topography data sets and models and identify the presence of terminal moraines at the grounding line of several fjords. These new bathymetry data can be used to gain insights into past locations of glacier grounding lines, as well as boundary conditions for the ice sheet [*Nick et al.*, 2009] and ocean models [*Heimbach and Losch*, 2012; *Padman et al.*, 2012; *Schodlok et al.*, 2012].

2. Data

Data for developing the new topography and bathymetry were collected by NASA's Operation IceBridge flights over Greenland during three field seasons, 2010, 2011, and 2012. Data were collected with NASA's
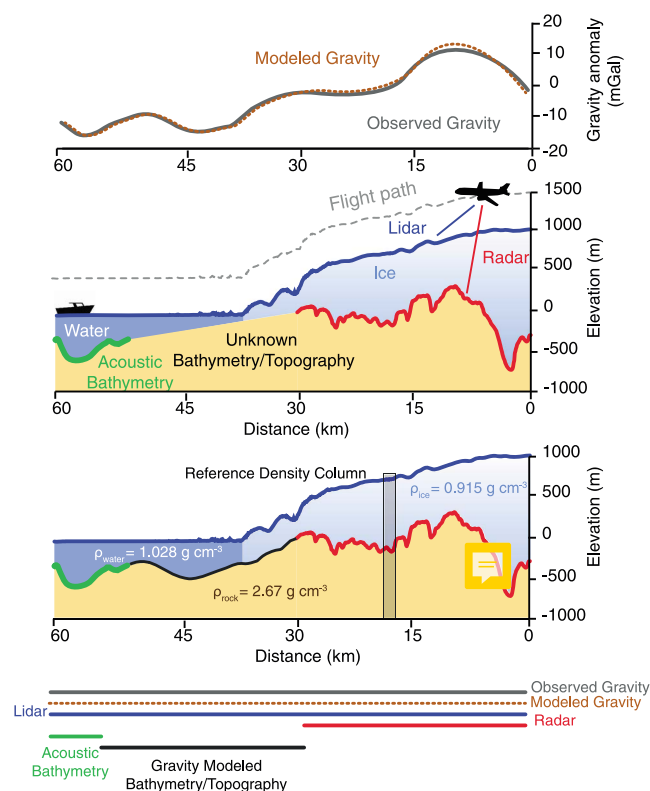
Figure 2. Schematic illustration of the gravity inversion procedure for modeling bathymetry and subice topography. (top) Observed and modeled gravity anomalies along a flow line profile. (middle) Draped flight geometry of the aircraft, data sets used for model constraints (airborne lidar and radar and marine-based acoustic bathymetry), and the typical gap in bathymetry and subice topography that exists in outlet glaciers. (bottom) Result of the inversion, with the black line representing the new bathymetry and topography resulting from the inversion. The densities and the reference density column are also shown.

DC-8 aircraft in 2010 and NASA's P-3 aircraft in all years. The aircraft flew a draped flight pattern (i.e., maintaining a constant nominal elevation of 500 m above the surface) (Figure 2). The average aircraft speed, as resolved with differential GPS, was ~250 kts for the P3 and 270–275 kts for the DC-8 [*Cochran and Bell*, 2010, updated 2014)].

The IceBridge instrument suite during this period included radar systems from the Center for Remote Sensing of Ice Sheets (CReSIS) for imaging the snow, ice, and subice topography; the NASA Airborne Topographic Mapper (ATM) laser altimeter for measuring the ice surface; and a gravimeter and magnetometer operated together by Sander Geophysics Ltd., the U. S. Geological Survey (USGS), and Lamont-Doherty Earth Observatory (Figure 2). The magnetometer was only available for flights in 2011 and 2012. All data sets are referenced to the WGS84 ellipsoid.

More than 400,000 line kilometers (km) of airborne data were acquired from 2010 to 2012 (Figure 1) including nearly 10,000 line of data along 87 distinct fjords. Over this period, IceBridge repeated lines along fjords in order to measure glacier elevation changes, resulting in a total of 211 along-fjord-axis flights. Multiple profiles were available along some of the glaciers and fjords. We produced gravity-based subglacial topography and fjord bathymetry in 90 profiles down 54 distinct glaciers and fjords (Figure 1). We have used the gravity inversion method to obtain 875 line kilometers of new subglacial topography and 1950 line kilometers of new fjord bathymetry in 54 distinct fjords. All IceBridge data sets are available at the National Snow and Ice Data Center (NSIDC) (http://nsidc.org/data/IceBridge/data_summaries.html).

2.1. Gravity

The Sander Geophysics Ltd. Airborne Inertially Referenced Gravimeter (AIRGrav) was used to measure the gravity field during the Greenland IceBridge missions from 2010 to 2012 [*Cochran and Bell*, 2010, updated 2014)]. The AIRGrav system measures all accelerations experienced by the aircraft, including accelerations due to variations in the Earth's gravity field, as well as those associated with the aircraft's motion. Aircraft accelerations are independently recorded using differential GPS measurements and are subtracted from the total accelerations recorded by the AIRGrav system.

Among airborne gravimeters, the AIRGrav system is uniquely capable of acquiring high-quality data during draped flights [*Studinger et al.*, 2008] and is able to distinguish variations in the Earth's gravity field that are on the order of tens of milliGals from aircraft accelerations that typically reach 100,000 mGal. The AIRGrav system consists of three orthogonal accelerometers with a three-axis gyro-stabilized inertial platform. The vertical accelerometer is the primary gravity sensor and is maintained within 10″ of the local vertical by the Schuler-tuned inertial platform, using the gyroscopes and two horizontal accelerometers [*Sander et al.*, 2004].
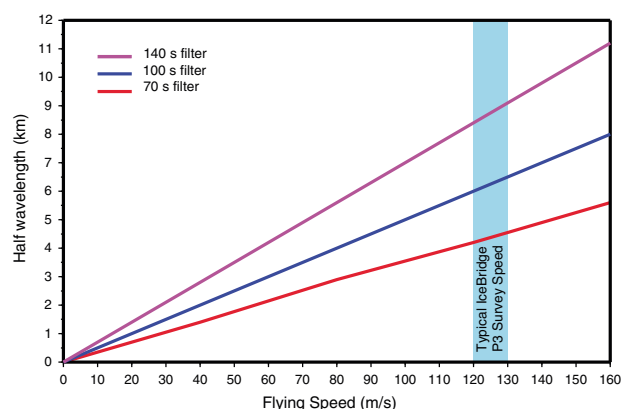
Figure 3. Aircraft speed versus resolution for measured gravity. The purple line shows the 140 s filter, the blue line shows the 100 s filter, and the red line shows the 70 s filter which we use in the inversions. The shaded blue region shows typical aircraft speed for the NASA P3, the aircraft used for the majority of the IceBridge surveys in Greenland from 2010 to 2012.

Corrections are applied to the raw gravity data to produce the free-air anomalies used in the bathymetry models. The predicted field is removed according to the international gravity formula 1980 formula [*Moritz*, 2000] (based on the WGS84 ellipsoid). Corrections are applied for the effects of measuring from a moving platform on a rotating Earth (Eötvös correction) and the survey height above the ellipsoid (free-air correction). The free-air anomaly data are filtered with full-wavelength filters of 70, 100, and 140 s widths. The analysis presented here uses the 70 s filter data. Accounting for both the filter and the speed of the aircraft, the 70 s filtered gravity data have an along-track half-wavelength resolution of 4.5 km (Figure 3). The amplitude of features narrower than ~5 km is not fully resolved by the gravity data.

2.2. Lidar

The surface elevation is measured by the Airborne Topographic Mapper (ATM) scanning laser altimeter [*Krabill*, 2014]. The ATM system is a conical range-finding laser that has measured the surface of the Greenland Ice Sheet since the 1990s [*Krabill et al.*, 1995]. The ATM surface elevations are the primary constraint on the ice surface in our models.

2.3. Radar

The CReSIS Multichannel Coherent Radar Depth Sounder (MCoRDS) radar provides measurements of ice thickness [*Allen et al.*, 2010]. Crossover analyses of ice thickness determinations give a repeatability of 10 m [*Gogineni et al.*, 2014; *MacGregor et al.*, 2015]. The radar returns for the Greenland campaigns analyzed here were either automatically detected or manually identified by CReSIS. Surface elevation measurements are given as ellipsoidal elevations, and the ice base is established by subtracting radar-derived ice thickness from ATM surface values.

From 2010 to 2012, MCoRDS retrieved ~4500 line kilometers of ice thickness measurements along ~6000 line kilometers of onshore data in the 90 profiles we analyzed. In northern Greenland, where the ice is colder, MCoRDS measures the ice thickness up to the grounding lines. Elsewhere in Greenland, radar gaps of up to 65 km can occur landward of the grounding line due either to warm ice that attenuates the radar signal or extensive fracturing that scatters the radar signal.

Gravity data were not collected on 2013 and 2014 OIB Greenland flights. However, when radar data from these two years are available along glaciers where we inverted gravity from previous years, we compared the radar-determined bed with the gravity-determined bed as part of our quality control. In three cases, we used 2014 radar that measured the bed much closer to the grounding line as an improved constraint for the inversions. These three glaciers are Upernavik North (Glacier #20) on the northwest coast and A.P. Berstorff (Glacier #147) and Heimdal (Glacier #151) in southeastern Greenland.

2.4. Magnetometer

Magnetic anomaly data were acquired with a Scintrex CS-3 cesium vapor magnetometer sensor and a Billingsley TFM100G2 fluxgate magnetometer during the 2011 and 2012 field seasons [*Cochran et al.*, 2012]. Base station data were acquired by the U.S. Geological Survey (USGS) with a GEM Systems GSM-19 Overhauser magnetometer using a 3 s sample rate at Thule or Kangerlussuaq as appropriate. International Real-time Magnetic Observatory Network (INTERMAGNET) observatories in Thule (THL), Godhavn (GDH), and Narsarsuaq (NAQ) were also used with a 1 min sample rate to monitor the diurnal variation over the duration of the flight.

Data were acquired at 100–160 Hz, then despiked and decimated to 20 Hz. Diurnal variations in the field were removed using the base station and INTERMAGNET data recorded during the flight. On long-baseline flights,

Table 1. Fjord Properties[a]

Name	ID	Grounding Line Depth (Ellipsoid) (m)	Grounding Line Depth (Geoid) (m)	Minimum Fjord Depth (Ellipsoid) (m)	Minimum Fjord Depth (Geoid) (m)	Maximum Fjord Depth (Ellipsoid) (m)	Maximum Fjord Depth (Geoid) (m)	Bathymetry Modeled (km)	Topography Modeled (km)
Jakobshavn Isbrae	**3**	**−613**	**−642**			**−1008**	**−1039**	**137**	**65**
3.120[b]	3	−613	−642			−1008	−1039	137	65
Eqip Sermia	**5**	**−319**	**−347**			**−433**	**−462**	**6**	**19**
5.120[b]	5	−319	−347			−433	−462	6	19
Store Gletscher	**9**	**−324**	**−354**			**−571**	**−600**	**11**	**23**
9.120[b]	9	−324	−354			−571	−600	11	23
Kangerlussuup Sermersua	**14**	**−61**	**−92**	**−50**	**−79**	**−392**	**−423**	**52**	**18**
14.100[b]	14	−61	−92	−50	−79	−392	−423	52	18
Rink Isbrae	**15**	**−577**	**−609**			**−1260**	**−1291**	**56**	**23**
15.100[b]	15	−577	−609			−1260	−1291	56	23
Umiammakku Isbrae	**16**	**−435**	**−466**			**−617**	**−647**	**30**	**54**
16.100	16	−481	−512			−568	−598	30	60
16.110	16	−422	−453			−597	−626	30	63
16.120[b]	16	−403	−433			−617	−647	31	54
Inngia Isbrae	**17**	**−331**	**−362**	**−329**	**−358**	**−659**	**−689**	**61**	**2**
17.100	17	−320	−351			−659	−689	51	
17.110[b]	17	−400	−432	−329	−358	−615	−645	61	2
17.120	17	−273	−304			−636	−666	44	
Upernavik Isstrom South	**18**	**−750**	**−776**	**−36**	**−660**	**−883**	**−907**	**44**	**20**
18.110	18	−709	−735			−818	−844	15	24
18.120[b]	18	−791	−817	−636	−660	−883	−907	44	20
Upernavik North	**20**	**−833**	**−858**	**−895**	**−920**	**−1168**	**−1194**	**26**	**2**
20.110	20	−908	−933	−895	−920	−1168	−1194	26	3
20.111[b]	20	−836	−862			−1119	−1145	22	2
20.120	20	−754	−780			−1112	−1137	25	5
Alison Gletscher	**31**	**−246**	**−269**	**−236**	**−259**	**−423**	**−446**	**24**	**8**
31.120[b]	31	−246	−269	−236	−259	−423	−446	24	8
Sverdrup Gletscher	**40**	**−528**	**−550**	**−368**	**−390**	**−528**	**−550**	**9**	
40.100[b]	40	−528	−550	−368	−390	−528	−550	9	
Nansen Gletscher	**41**	**−378**	**−400**	**−146**	**−167**	**−378**	**−400**	**7**	
41.100[b]	41	−378	−400	−146	−167	−378	−400	7	
Kong Oscar Gletscher	**44**	**−777**	**−798**	**−548**	**−569**	**−777**	**−798**	**13**	
44.120[b]	44	−777	−798	−548	−569	−777	−798	13	
Rink Gletscher	**48**	**−249**	**−270**			**−667**	**−689**	**33**	**1**
48.120[b]	48	−249	−270			−667	−689	33	1
Yngvar Nielsen Brae	**55**	**−324**	**−345**	**−305**	**−327**	**−488**	**−508**	**19**	
55.100[b]	55	−343	−364			−488	−508	19	
55.110	55	−322	−343			−426	−447	19	
55.111	55	−308	−329	−305	−327	−454	−473	16	
Savissuaq Gletscher	**57**	**−227**	**−248**			**−524**	**−543**	**27**	**13**
57.110	57	−246	−267			−458	−477	12	13
57.120[b]	57	−208	−228			−524	−543	27	16
Nigerlikasik	**58**	**−208**	**−227**			**−331**	**−349**	**4**	**10**
58.110	58	−215	−233			−331	−349	4	10
58.120[b]	58	−201	−220			−246	−264	3	10
Heilprin Gletscher	**63**	**−363**	**−383**	**−277**	**−297**	**−631**	**−651**	**38**	
63.100[b]	63	−336	−356	−277	−297	−419	−439	13	
63.120	63	−406	−426	−304	−324	−461	−481	12	
63.121	63	−346	−366	−313	−333	−631	−651	25	
Tracy Gletscher	**64**	**−604**	**−624**	**−370**	**−390**	**−826**	**−846**	**43**	**8**
64.100	64	−608	−629			−826	−846	17	
64.110[b]	64	−648	−668			−668	−688	13	
64.120	64	−640	−660			−728	−748	16	
64.121	64	−520	−540	−370	−390	−802	−821	25	8
Humboldt Gletscher	**70**	**−193**	**−206**			**−227**	**−239**	**19**	
70.120[b]	70	−193	−206			−227	−239	19	
Newman Bugt	**71**	**−184**	**−202**			**−256**	**−274**	**38**	

Table 1. (continued)

Name	ID	Grounding Line Depth (Ellipsoid) (m)	Grounding Line Depth (Geoid) (m)	Minimum Fjord Depth (Ellipsoid) (m)	Minimum Fjord Depth (Geoid) (m)	Maximum Fjord Depth (Ellipsoid) (m)	Maximum Fjord Depth (Geoid) (m)	Bathymetry Modeled (km)	Topography Modeled (km)
71.120[b]	71	−184	−202			−256	−274	38	
Steensby Gletscher	**72**	**−333**	**−352**	**−51**	**−69**	**−333**	**−352**	**22**	
72.110[b]	72	−333	−352	−51	−69	−333	−352	22	
Ryder Gletscher	**73**	**−567**	**−589**	**−374**	**−395**	**−937**	**−957**	**39**	
73.110[b]	73	−567	−589	−374	−395	−937	−957	39	
C.H.Ostenfeld gletscher	**75**	**−497**	**−523**	**−382**	**−407**	**−772**	**−1424**	**78**	
75.120[b]	75	−497	−523	−382	−407	−772	−1424	78	
Marie Sophie gletscher	**78**	**−178**	**−211**			**−876**	**−907**	**84**	
78.120[b]	78	−178	−211			−876	−907	84	
Academy Gletscher	**79**	**−280**	**−314**			**−1265**	**−1296**	**93**	
79.120	79	−271	−305			−692	−725	15	
79.121[b]	79	−289	−323			−1265	−1296	93	
Hagen Brae	**80**	**−190**	**−224**	**−134**	**−165**	**−424**	**−479**	**55**	
80.110[b]	80	−190	−224	−134	−165	−424	−479	55	
Zachariae Isstrom	**82**	**−615**	**−493**	**−448**	**−476**	**−1008**	**−1072**	**115**	
82.102	82	−581	−609	−448	−476	−705	−795	25	
82.103[b]	82	−348	−376			−744	−777	34	
82.110	82					−1008	−1072	22	
82.111	82					−890	−918	23	
82.120	82					−590	−628	11	
Gerard de Geer Gletscher	**88**	**−303**	**−351**						**30**
88.120[b]	88	−303	−351						30
Morell Gletscher	**90**	**−440**	**−488**	**−33**	**−82**	**−495**	**−545**	**30**	**4**
90.120[b]	90	−440	−488	−33	−82	−495	−545	30	4
F. Graae Gletscher	**91**	**−508**	**−560**	**−267**	**−319**	**−1326**	**−1377**	**88**	
91.120[b]	91	−508	−560	−267	−319	−1326	−1377	88	
Daugaard−Jensen	**92**			**−726**	**−777**	**−1184**	**−1236**	**43**	**23**
92.110[b]	92			−726	−777	−1184	−1236	43	23
Sydbrae	**101**	**−374**	**−430**			**−455**	**−511**	**2**	**6**
101.120[b]	101	−374	−430			−455	−511	2	6
Bredegletscher	**102**	**−268**	**−324**			**−452**	**−508**	**4**	**3**
102.120[b]	102	−268	−324			−452	−508	4	3
Dendritgletscher	**104**	**−69**	**−129**						**82**
104.120[b]	104	−69	−129						82
Midgaard Gletscher	**131**	**−55**	**−108**	**−152**	**−204**	**−421**	**−477**	**33**	**67**
133.120	131	−55	−108	−152	−204	−421	−477	33	67
Helheimgletscher	**133**	**−620**	**−670**	**−125**	**−176**	**−637**	**−687**	**47**	**12**
133.110	133	−637	−687	−508	−558	−637	−687	13	34
133.111	133			−125	−176	−564	−614	30	20
133.120[b]	133	−611	−661	−293	−343	−604	−654	47	12
133.121	133	−612	−662	−437	−488	−612	−662	28	16
Ikertivaq North	**135**					**−522**	**−569**	**17**	
135.120[b]	135					−522	−569	17	
Koge Bugt	**140**	**−385**	**−432**	**−231**	**−277**	**−578**	**−624**	**46**	
140.120[b]	140	−385	−432	−231	−277	−578	−624	46	
Umiivik Fjord	**144**	**−136**	**−181**	**−80**	**−126**	**−178**	**−223**	**11**	**34**
144.120[b]	144	−136	−181	−80	−126	−178	−223	11	34
Graulv	**145**	**−290**	**−338**	**−268**	**−315**	**−641**	**−688**	**26**	**9**
145.101	145	−225	−272			−369	−416	16	10
145.110[b]	145	−294	−342	−268	−315	−507	−554	24	9
145.111	145	−352	−400	−333	−380	−641	−688	26	9
A.P. Bernstorff Gletscher	**147**	**−598**	**−645**	**−401**	**−447**	**−969**	**−1053**	**40**	**15**
147.100	147	−694	−741	−579	−626	−627	−673	8	20
147.110	147	−579	−626			−824	−871	29	15
147.111	147	−549	−596			−884	−930	19	16
147.120	147	−668	−715	−401	−447	−1006	−1053	40	16
147.121[b]	147	−501	−548	−427	−473	−858	−904	39	16
Skinfaxe	**149**	**−99**	**−145**			**−180**	**−226**	**5**	**56**

Table 1. (continued)

Name	ID	Grounding Line Depth (Ellipsoid) (m)	Grounding Line Depth (Geoid) (m)	Minimum Fjord Depth (Ellipsoid) (m)	Minimum Fjord Depth (Geoid) (m)	Maximum Fjord Depth (Ellipsoid) (m)	Maximum Fjord Depth (Geoid) (m)	Bathymetry Modeled (km)	Topography Modeled (km)
149.120[b]	149	−99	−145			−180	−226	5	56
Heimdal Gletscher	**151**	**−312**	**−359**						**12**
151.101[b]	151	−312	−359					2	12
151.110	151								15
Kangiata Nunaata Sermia (KNS)	**160**	**−140**	**−174**			**−353**	**−385**	**34**	**28**
160.100	160	−125	−159			−353	−385	29	29
160.110[b]	160	−136	−170			−331	−363	34	29
160.120	160	−159	−193			−282	−315	27	28
Akullersuup Sermia	**161**			**−153**	**−185**	**−504**	**−535**	**35**	**37**
161.110[b]	161			−153	−185	−504	−535	35	37
Narsap Sermia	**162**	**−288**	**−320**			**−676**	**−707**	**5**	**51**
162.100[b]	162	−288	−320			−676	−707	5	51
Petermann Gletscher	**193**	**−534**	**−551**	**−200**	**−212**	**−1254**	**−1266**	**118**	
193.110[b]	193	−534	−551	−200	−212	−1254	−1266	118	
Docker Smith Gl. West	**194**	**−332**	**−353**	**−211**	**−232**	**−332**	**−353**	**18**	**7**
194.120[b]	194	−332	−353	−211	−232	−332	−353	18	7
Puisortoq North	**200**								**39**
200.120[b]	200								39
Saqqap Sermersua	**207**							**14**	**51**
207.100	207								75
207.110[b]	207					−183	−213	14	51
Upernavik Northwest	**301**	**−153**	**−179**			**−644**	**−670**	**7**	**2**
301.110[b]	301	−135	−161			−644	−670	7	2
301.11	301	−206	−232			−260	−285		2
301.112	301	−119	−145			−659	−684	7	5
Nioghalvfjerdsfjorden (79 North)	**500**	**−518**	**−548**	**−133**	**−164**	**−969**	**−999**	**70**	
500.101[b]	500	−518	−548	−133	−164	−969	−999	70	
Puisortoq South	**700**	**−247**	**−293**	**−117**	**−163**	**−399**	**−446**	**27**	**38**
700.120[b]	700	−247	−293	−117	−163	−399	−446	27	38

[a]Rows in bold show average grounding lines, minimum, and maximum fjords depths for all models along the fjords.
[b]Models in the supporting information.

multiple base stations were applied using the method of *Smith et al.* [2014]. Changes in the magnetic field resulting from aircraft maneuvers and heading changes were compensated for by compensation corrections [*Leliak*, 1961; *Noriega*, 2011] derived with PEIComp software. Compensation coefficients were established from box patterns flown at high elevation in magnetically quiet regions located close to both Thule and Kangerlussuaq. Magnetic anomalies were established by subtracting the field predicted by the International Geomagnetic Reference Field from the observed field.

2.5. Measurement Reference Frame

The modeled bathymetry from the Operation IceBridge data is given with respect to the WGS84 ellipsoid and is consistent with all IceBridge data sets used in the model development.

A geoid correction must be applied to the modeled bathymetry elevations in order to recover actual water depth. Around the coast of Greenland, the geoid is consistently higher than the ellipsoid by approximately 20 m in the northwest and 50 m in the southeast [*Forste et al.*, 2008]. The actual water depths can differ from the ellipsoidal elevations given in these bathymetry models by 20–50 m. Table 1 presents both actual water depths and ellipsoidal elevations.

3. Methodology

The free-air gravity data reflect the distribution of mass beneath the aircraft with a positive anomaly indicating excess mass and a negative anomaly indicating a mass deficit relative to a theoretical gravity field. The gravity
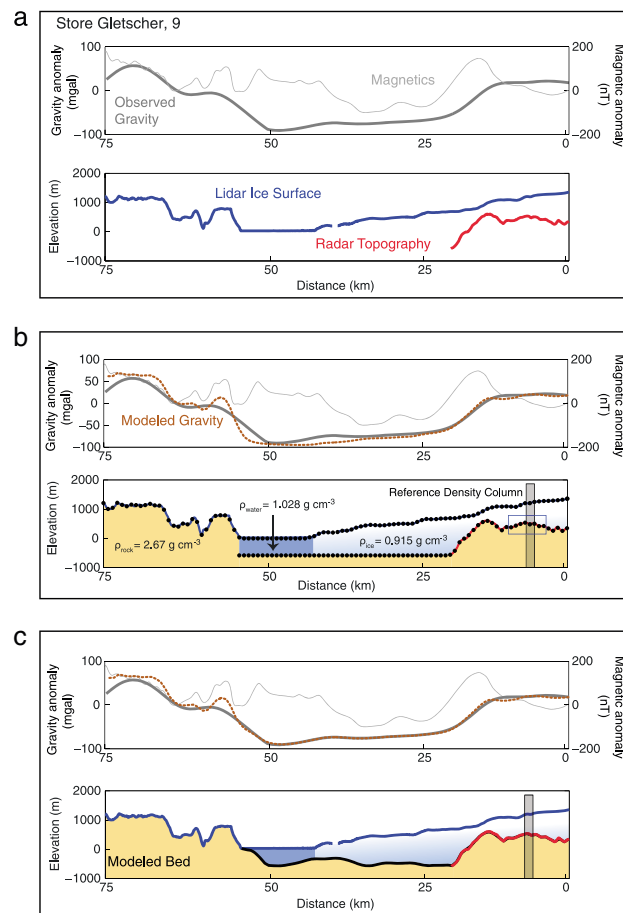
Figure 4. Model procedure illustrated using Store Glacier (Glacier 9). (a) IceBridge constraints: lidar ice surface, radar ice thickness, gravity, and magnetic data. The model has offshore lidar constraints where the aircraft flew over rock. (b) Forward model with three major density bodies constrained by IceBridge measurements. The black dots indicate horizontal resolution of the model. The points in the blue box show suitable reference density column selections based on the criteria discussed in the text, and the shaded rectangle shows selected reference density column. The dashed red line shows forward modeled gravity for the known constraints and unknown bed. (c) Final model with constraints and inverted bathymetry and topography.

inversion process exploits this relationship to model topography. We inverted the gravity signal to derive the topography on the density interface between ice and rock or water along the fjord axis.

We modeled only the fjord axis flights where adequate gravity data were measured (Figure 1). Along each profile, we employed radar returns as far upstream as the 50 m/yr ice velocity contour [*Rignot and Mouginot*, 2012]. We used the observed data to produce a preliminary forward model of the gravity field. We examined the match between the observed and forward modeled gravity and selected an appropriate reference density column, which is required to define the offset between the calculated and observed gravity data. We inverted the free-air gravity anomaly data where the bathymetry and subice topography were unknown. Finally we fine tuned the models to remove model artifacts. We applied this consistent technique to the 90 profiles presented in Table 1. These 90 profiles are available at NSIDC. Insights from the regional geology, magnetic data, long-wavelength anomalies, and crossing or reoccupied flight lines were considered when appropriate on a model-by-model basis.

3.1. Data Assimilation and Forward Modeling

We assembled all the IceBridge data along each profile in a single database (Figure 4a). These data include free-air gravity, radar, lidar, magnetic, and offshore shipboard bathymetry measurements where available. All data sets were subsampled at 2 Hz and aggregated, providing a surface-to-base view of the ice sheet for each flight line. Additional data sets were used in the modeling process in some cases. These data sets include gravity anomaly data from the World Gravity Map (WGM2012) [*Balmino et al.*, 2012; *Bonvalot et al.*, 2012], and existing offshore bathymetry data [e.g., *Johnson et al.*, 2011; *Mortensen et al.*, 2011, 2014; *Schumann et al.*, 2012].

The inverse gravity method produces inherently nonunique solutions. We limit the number of possible solutions based on knowledge of the physical properties and structure of the Earth. We use information about the range of possible rock densities in Greenland and impose the reasonable condition that the solution cannot have unrealistic topography or subsurface structure. In section 4 where we discuss uncertainty, we investigate the effects of changing parameters within the limits of what is typically observed in nature.

Before calculating the forward model, we conducted a basic quality control of the IceBridge data used for model horizons. At locations where ATM ice surface elevation data were not available, we used MCoRDS ice surface measurements. ATM has a higher vertical resolution than MCoRDS. An offset of up to ~3 m can

occur between the two measurements and was removed in each profile by leveling the MCoRDS ice surface to match the ATM ice surface.

We then merged high-quality and reduced-quality gravity data where appropriate. Reduced-quality data may be due to winding flight paths which introduce additional horizontal accelerations into the raw data. Where horizontal accelerations exceed defined thresholds, the measurements are flagged as reduced quality or as unusable, introducing gaps in the IceBridge gravity data sets archived at NSIDC. Since the high- and reduced-quality data are processed and filtered independently, an offset of up to 2–3 mGal between the two may be present. We removed the offset by shifting the reduced quality data to the level of the high quality data. Although the vast majority of the data collected by IceBridge is high quality, challenging conditions resulted in reduced quality gravity for approximately half of the data used in the models. There are also numerous lines where the combination of a winding flight path and turbulence resulted in insufficient usable data to produce a model. Data quality was sufficient to produce 90 models for the glaciers and fjords surveyed by OIB in 2010–2012.

We used the Geosoft GMSys software package to calculate the forward modeled gravity (Figures 4a and 4b). The forward modeled gravity field was calculated based on the known radar and lidar constraints of three bodies, each with homogenous densities. The bodies are the underlying bedrock (2.67 g/cm^3), the ice sheet and floating tongues (0.915 g/cm^3), and the water (1.028 g/cm^3). In the initial models, we assumed that the fjords contained no sediment and discuss this assumption below. To avoid introducing edge effects into the modeled bathymetry, the model space extended 30,000 km along the profile at both ends to 50 km depth and to infinity orthogonal to the profile.

A reference density column within each model is necessary to define the offset between the calculated and observed gravity data. We used four criteria to determine the location of the reference density column along the profile (Figure 4b). The criteria are the following: (1) the ice surface and subice topography are constrained by lidar and radar, respectively, (2) the sub ice topography is relatively flat, (3) the root-mean-squared (RMS) error along the entire profile between the forward modeled gravity and observed gravity over grounded ice where the bed is observed in the radar is minimized, and (4) proximity to the grounding line. A reference density column close to the grounding line best represents the density distribution in the lower reaches of the glacier and in the fjord.

The preliminary model produced a modeled gravity anomaly (Figure 4b) that always differed from the observed gravity. These differences, or residual gravity anomalies, occurred where the bathymetry and subice topography were unknown and assumed to be flat and they reflected the mass surplus or deficit from the missing bathymetry or topography absent from the preliminary model.

3.2. Invert for Bathymetry and Fine Tune

The next step was to invert the gravity in regions where bathymetry and subice topography were unconstrained and produced residuals in the forward model. We employed the GMSys software package which uses an iterative approach based on the method of *Talwani et al.* [1959] to model bathymetry and subice topography and calculate the gravity anomaly from the inversion.

We fine tuned the models to correct for spikes introduced in the initial inversion and for large residuals. We manually smoothed these points and ran the inversion again. We also evaluated the radar bed identifications in locations with very large residuals. We eliminated any ambiguous MCoRDS bed identifications that caused high residuals and reran the inversion.

The final models have bathymetry and topography that follow the shape of the gravity anomaly with minimized residuals (Figure 4c). At this stage we evaluated the quality of the models based on local geology and offshore bathymetric constraints.

4. Uncertainty

Uncertainty in bathymetry models comes from instrument uncertainty, model resolution, model procedure, and along-profile changes in geology. Together these factors introduce uncertainty in the absolute elevations of the modeled bathymetry and topography. We estimate the total uncertainty budget to range from 90 to 110 m (Table 2). The overall shape of the bathymetry resulting from the inversion is more reliable than the absolute elevation.

Table 2. Uncertainty and Model Sensitivity[a]

Instrument and Model Procedure		
Source	Measurement	Uncertainty (m)
Gravity	0.72–2 mGal	10–28
Lidar	0.01 m	0.05
Radar	10 m	10
Model Procedure		33
Total		53–71

[a]Sensitivity of model results to rock density is 5 m for 0.01 g/cm3 density change. Sensitivity of model results to sediment is 30 m for 100 m of sediment thickness.

4.1. Instrument Accuracy

The gravity inversion for bathymetry and topography depends on the gravity, radar, and lidar measurements. The uncertainty in each of these measurements contributes to the error in the final bathymetry and topography models. The gravity and radar accuracies are the two largest sources of instrument uncertainty (Table 2).

4.1.1. Uncertainties in Gravity Measurements

Errors in gravity measurements may be assessed either by analyzing reoccupied profiles or by crossover analysis. Reoccupied profiles give a better estimate of the repeatability and along-track reliability of gravity measurements because of the along-track directionality of the time filtering applied to the gravity anomalies. The consequence of this along-track directional filtering is that the gravity value at a particular point will be influenced by measurements within a half filter width in each direction along the track. Because this filter is applied along track, lines that cross each other orthogonally will show a greater mismatch at their crossing point than lines that reoccupy the same paths. *Cochran et al.* [2011] found that the RMS gravity difference at crossing points for all Arctic IceBridge campaigns from 2010 to 2011 increased from 2.25 mGal for a 70 s full-wavelength filter to 3.56 mGal for a 140 s filter. The increase in the mismatch with increasing filter length is the result of directional filtering. In contrast, they found that the RMS gravity differences for reoccupied flight paths in the Arctic decreased from 0.72 mGal for a 70 s full-wavelength filter to 0.47 mGal for a 140 s filter. We use these latter values in our error analysis because they are better estimates of the repeatability and along-track accuracy of the gravity data in the fjords. Analysis of repeat tracks of reduced quality data along Petermann Glacier show an RMS difference of 2.0 mGal. A simple Bouguer slab calculation indicates that a range of 0.72–2.0 mGal uncertainty in the gravity anomaly translates into an approximately 10–28 m uncertainty in the modeled bathymetry/topography.

4.1.2. ATM Altimeter Uncertainties

Based on comparison of measurements from crossing paths, the accuracy of ice surface measurements from the ATM system is estimated to be on the order of 10 cm independent of the reflecting surface (rock, ice, or water) [*Martin et al.*, 2012]. The uncertainty in ATM ice surface measurements does not significantly contribute to uncertainty in the models.

4.1.3. MCoRDS Radar Uncertainties

Ice thickness measured by the MCoRDS system is a critical measurement for the gravity inversion, since we use the radar-constrained bed in the choice of a reference density column. Uncertainty in the MCoRDS subice topography is about 10 m [*Gogineni et al.*, 2014; *MacGregor et al.*, 2015]. This radar uncertainty directly translates to a 10 m uncertainty in the final gravity-based bathymetric models. The bed is identified from the radar echogram, either manually or with a computer algorithm, so an additional uncertainty can arise from ambiguous or unclear returns that can result in erroneous choices for the bed location.

4.2. Changes in Geology

The bedrock of Greenland is predominantly Precambrian crystalline shield rocks, primarily gneisses, and high-grade metasediments developed during a series of orogenic events that ended 1.6 Ga ago [*Henriksen et al.*, 2009]. Thick sedimentary deposits along the oceanic margins of the Precambrian craton were deformed and metamorphosed during the Paleozoic closing of those oceans, resulting in the Devonian Ellesmerian fold belt in northernmost Greenland and the Ordovician/Devonian Caledonides in eastern Greenland [*Henriksen et al.*, 2009]. Rifting to form the Labrador Sea and the North Atlantic in the early Cenozoic resulted in the emplacement of thick sequences of basaltic rocks along portions of both the western and eastern margins of Greenland.

In the process of developing the gravity-based bathymetry and topography, we assume that the density of the underlying rocks is constant and the geology is homogeneous. We adopt a constant rock density of 2.67 g/cm^3
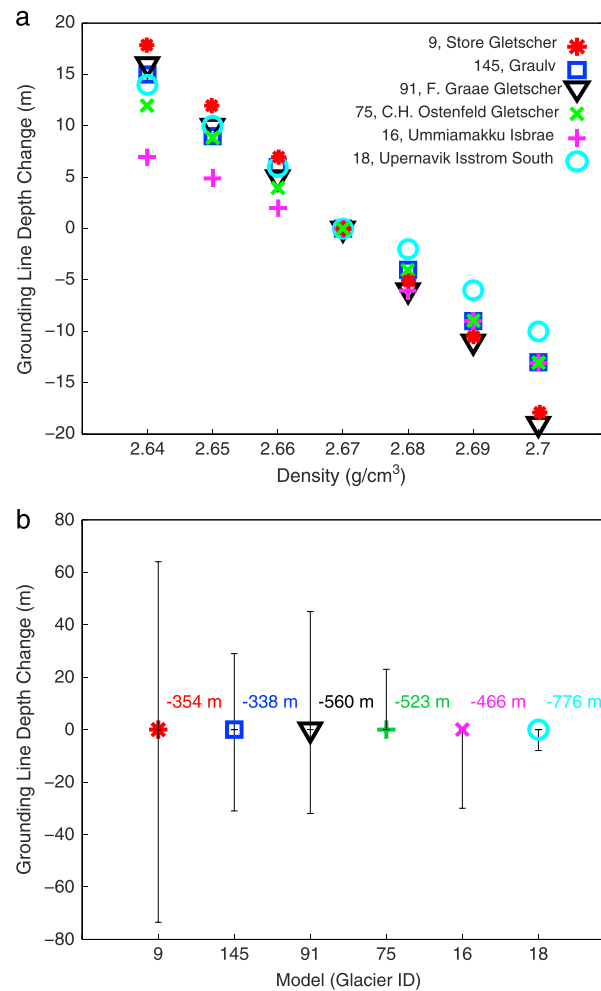
Figure 5. Effect of rock density variations and reference density column location on modeled bathymetry for a subset of models, Store (Glacier 9), Umiammakku Isbrae (Glacier 16), Upernavik Isstrom South (Glacier 18), Graulv (Glacier 145), F. Graae Gletscher (Glacier 91), and C. H. Ostenfeld Gletscher (Glacier 75). (a) Change in the grounding line depth resulting from varying rock density from 2.64 to 2.7 g/cm³. A 0.01 g/cm³ change in rock density results in an ~5 m change in grounding line depth. (b) Change in the grounding line depth as a result of changing the reference density column location within the criteria given in the text. The grounding line depth for our preferred location is noted for each glacier.

as representative of the Greenland rock density. This value of 2.67 g/cm³ has been a standard crustal density for gravity modeling since the pioneering isostatic surveys of the U. S. Coast and Geodetic Survey found that it minimized isostatic anomalies [e.g., *Hayford and Bowie*, 1912]. The densities of shallow crustal rocks do vary, generally within a range of about 2.6 g/cm³ to 2.8 g/cm³ [e.g., *Dobrin*, 1976; *Telford et al.*, 1990]. Volcanic terrains, as found along the eastern continental shelf of Greenland, may have densities as high as 2.9 g/cm³. Due to the horizontal resolution of the gravity data, local heterogeneity on the scale of a few kilometers will not greatly affect the modeling, as long as the average density remains reasonably constant. This average density may, however, vary from our assumed density of 2.67 g/cm³.

We consider two possible sources of density uncertainty. A homogeneous density uncertainty results from an average density that varies from our assumed density of 2.67 g/cm³. A heterogenous density uncertainty is the result of the modeled profile crossing a geological boundary that is associated with a change in average density. This heterogeneous density change occurs, for example, in southeast Greenland, where Archaean or Paleoproterozoic terrains onshore are adjacent to higher density Cenozoic volcanic flows and sills offshore.

4.2.1. Homogenous Density Change
In order to assess the model's sensitivity to our choice of rock density, we modeled the bathymetry for several typical profiles using a range of rock densities (Figure 5a). We changed the rock density by 0.01 g/cm³ intervals and noted changes in the model grounding line depth. For six typical glacier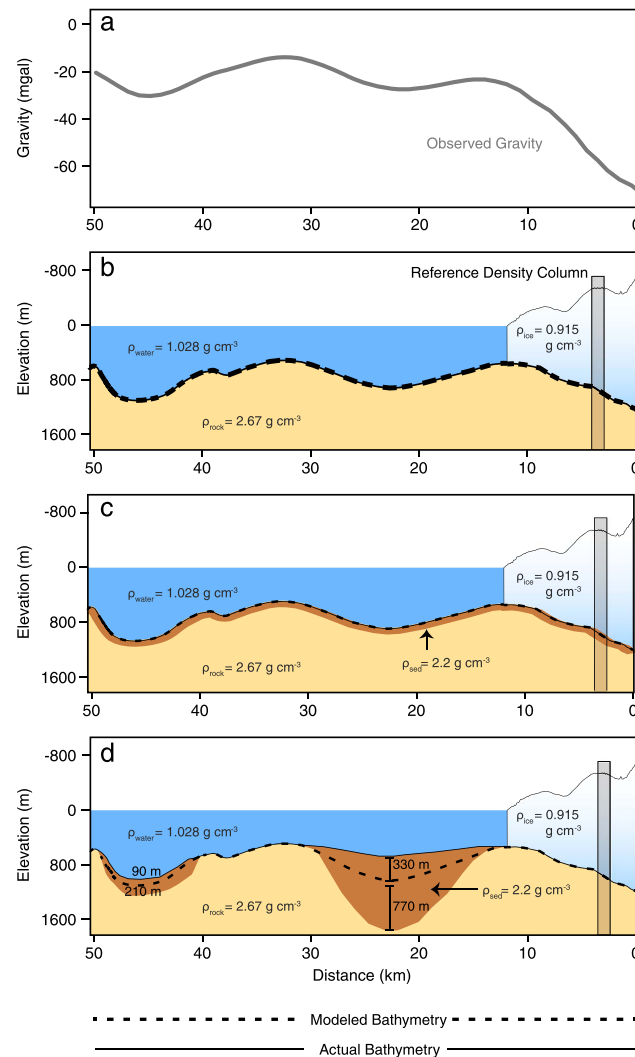s around Greenland, the grounding line depth varied by ~5 m for every 0.01 g/cm³ change in rock density (Figure 5a). This translates into a maximum difference of ~50–70 m from the grounding line determined with our assumed density over the entire probable density range. For comparison, *Cochran et al.* [2014] found that varying the crustal density by ±0.1 g/cm³ on the inversion of a profile along the axis of the Abbot Ice Shelf in Antarctica led to a maximum difference of 65 m in the resulting bathymetry beneath the ice shelf.

4.2.2. Heterogeneous Density Change
The rock density can also vary along the profiles if the profile passes from one formation to another with a different average density. The presence of geologic and density boundaries can be inferred where the inversion matches the radar-determined depth to bedrock along some portions of a profile but differs in other portions. The exact location of these geologic boundaries can be difficult to locate because the boundaries are often covered by ice or water. When possible, we use the magnetic data, in conjunction with existing geologic mapping [e.g., *Henriksen et al.*, 2009] to constrain the location of the geologic boundary and the nature of the density

Figure 6. Effect of sediment on gravity-based bathymetry models. (a) Observed gravity. (b–d) Different distributions of sediment in the fjord that would result in the same gravity signal. The solid black line shows the actual bathymetry, and the dotted black line shows the modeled bathymetry in all three cases. (Figure 6b) Case when there is no sediment. (Figure 6c) Case when there is a uniform sediment drape. Since the sediment is of a uniform thickness, the reference density column accounts for the sediment thickness. (Figure 6d) Case when there are pockets of sediment in the fjord not present at the reference density column location. This will cause the models to overestimate fjord depths in the sedimented area.

variation. A detailed discussion of this process is presented for Petermann Fjord by *Tinto et al.* [2015]. At Petermann, as well as at other fjords in northern Greenland, magnetic anomalies were used to define the boundary between the clastic metasediment of the Paleozoic Franklin Basin and less dense Silurian carbonate reefal sediment. Magnetic anomalies were extensively utilized to locate geologic boundaries in fjords in southeastern Greenland. Lines cross at their seaward ends from typical Archaean basement onto thick higher-density Cenozoic flood basalts and mafic intrusions [e.g., *Hopper et al.*, 2003; *Korenaga et al.*, 2000; *Nielsen*, 1987] at their seaward ends. The density change creates unrealistically shallow modeled bathymetry and large residuals at the seaward end of the profiles. We utilized magnetic anomalies to identify the location of the geologic boundary. We truncated the models at the geologic boundary and in the absence of marine constraints do not present modeled bathymetry seaward of the boundary.

The presence of sediment is another example of changing rock density along a profile. Glacial fjord sediment can range from a scoured bedrock floor to thick sediment accumulations (Figure 6). Due to lack of constraints on sediment thickness, we initially assumed there was no sediment in the fjords (Figure 6a).

The fjords in Greenland are likely to contain a layer of sediment as well as accumulations of ponded sediments filling depressions and mounds of sediment deposited during glacial retreat [*Syvitski and Shaw*, 1995] (Figures 6c and 6d). Where sediments in glacial fjords have been mapped, they are ten to hundreds of meters thick [*Syvitski and Shaw*, 1995]. In the case of

a uniform sediment drape, the gravity models may still correctly predict the subice topography and bathymetry in the fjord (Figure 6c). Since reference density columns are chosen very close to the grounding line, they will reflect the density structure including sediment accumulation across the grounding line (Figure 6c).

If a fjord contains an area with thicker sediment than the reference density column (Figure 6d), the modeled bathymetry will be deeper than the actual bathymetry. A simple Bouger slab calculation shows that the presence of an extensive layer of sediment will cause the calculated seafloor to be deeper than the actual bathymetry by a maximum of about 30 m for each 100 m of sediment with a density of 2.2 g/cm^3 [*Cochran and Bell*, 2012]. Narrow pockets of sediment will have less effect on the calculated depth. If the reference density column contains an accumulation of sediment that thins into the fjord, the modeled bathymetry will be shallow by the same factor.

4.3. Model Resolution

The primary control on model resolution is the along-track time domain filter applied to the gravity data as a part of the processing. The free-air gravity data at NSIDC are available with three different filters (70 s, 100 s, and 140 s). After testing our model procedure with each filter, we chose to use the 70 s filtered data for our inversions. The selection accepts slightly greater uncertainty in return for the significantly greater resolution. Since the filtering is done in the time domain, the resolution depends on the aircraft speed. Figure 3 shows the half-wavelength resolution as a function of flying speed for the three different filters. For a typical P3 flying speed of 250 kts (~125 m/sec), the half-wavelength resolution is 4.5 km. Narrower features will be present in the data but with a reduced amplitude and increased horizontal extent.

We define 100 evenly spaced nodes for the inversion along the unconstrained portion of a flow line profile. The average node spacing is ~1 km, which is higher than the resolution of the gravity data. The altimetry and radar data used to define the surface elevation and base of the ice also have resolutions that are much higher than the gravity, as does offshore shipboard bathymetry. The inherent resolution of the gravity data, defined by the aircraft speed and filter length, is the limiting factor in the resolution of the derived bathymetry and topography.

4.4. Reference Density Column

The selection of a reference density column for each profile is crucial. We varied the reference density column location in a set of typical glaciers from all around Greenland to assess the associated model uncertainty (Figure 5b). The six glaciers evaluated reflect the observed range of roughness in the radar-derived bed, which is a first-order control on how a change in the reference density column will affect the models.

For each of the six representative glacier/fjord profiles, we inverted the gravity to obtain bathymetry with different reference density column locations that met the criteria given in section 3.1. We used the variation in the grounding line depth as a metric of change. The change in the grounding line depth, as the reference density column position was moved, varied from 8 to 75 m for the six glaciers, with a mean change of 33 m (Figure 5b).

4.5. Summary

Summing all our instrument uncertainty estimates, uncertainty estimates from the model procedure, and accounting for the model's sensitivity to geological changes, we estimate the uncertainty in the models to range from 90 to 110 m (Table 2). The overall shape of the bathymetry, including factors such as the presence, relative amplitude, and location of sills, is more reliable than the absolute depths.

5. Results and Discussion

NASA's Operation IceBridge flew along 87 distinct fjords over the course of three years (2010–2012) during which gravity data were collected (Figure 1). Over this period, 211 along-fjord-axis lines were flown, including reoccupied flights. We applied a consistent gravity modeling technique to these lines and produced 90 models along 54 distinct fjords (Table 1). When there were multiple lines along a glacier or fjord, we modeled reoccupied lines as they are valuable for intermodel comparison. We also modeled noncoincident lines, which provide greater spatial coverage, particularly in open water. The results of this study provide a total of 1950 line kilometers of new bathymetry and 875 line kilometers of new subglacial topography.

In the supporting infromation, we present our preferred model for each fjord and discuss the results of the gravity inversions on a region-by-region basis. Our preferred model solution has smooth bathymetry and topography, a low-RMS error between observed and calculated gravity, and topographic shapes that match those of the gravity signal (Figure 2). We also take into account agreement with offshore bathymetry measurements and attempt to maximize the total length of new bathymetry modeled.

The primary goal of the gravity inversions is to provide bathymetry and subglacial topography in previously unmapped fjords in Greenland. The inversions enable us to identify important features of the glaciers and fjords, such as the grounding line depths and minimum and maximum water depths. Minimum water depths are considered important, as they obstruct relatively warm deep water from reaching the glacier.

For each fjord, we present a minimum water depth only in cases where a selection is appropriate. We do not report minimum water depths that occur in open water beyond the fjord or where the flight path crosses an island or turns to cross a fjord. We do not report a minimum fjord depth if the grounding line has the shallowest depth in the fjord. Where multiple profiles have been modeled in a fjord, we report the minimum and maximum water depths across all profiles (Table 1). In the modeled data set, there are nine fjords whose minimum water depths are shallower (i.e., a difference of over 200 m) than their grounding line depths (Table 1).

Since these new bathymetric models fill in a data gap between onshore and offshore constraints, the gravity inversions provide new grounding line depths for 12 of the surveyed glaciers. The position of the grounding line was determined based on a hydrostatic approximation. Sea level was based on the GL04C geoid [*Forste et al.*, 2008], and the altimetry for each model was corrected to the geoid. Where radar images the ice thickness at the grounding line, we report those depths in the model results. When there are multiple flights down a single fjord, we average the grounding line depths from each model (Table 1) since repeat flights typically cross the grounding line within 100 m of each other.

As previously mentioned, the along-profile subice topography and bathymetry data sent to NSIDC are given with respect to the ellipsoid in order to be consistent with IceBridge data sets. The depths discussed in this text are actual water depths, i.e., depths with respect to the geoid.

The gravity models presented here give new insights into the morphology of Greenland fjords and highlight the strength of IceBridge data sets when they are considered together. In this section we discuss geological changes along the profiles, including deep-sourced anomalies and the identification of sediment in certain fjords. We also illustrate how the gravity models can be used to assist the interpretation of radar data.

5.1. Deep-Sourced Anomalies

Deep density contrasts, arising from changes in crustal thickness or lateral variation in deep crustal or mantle densities, can introduce long-wavelength signals into the observed gravity. These deep density contrasts are identified where the forward model of the gravity anomaly over known subglacial topography has a different slope from the observed gravity anomaly.

An example of these long-wavelength anomalies is seen in the model for Petermann Glacier (Figure S7 in the supporting information, 193.110). Here when a reference density column is selected under grounded ice for the forward modeling step in the inversion (Figure 4b), the predicted gravity offshore in the area where the bathymetry is known from shipboard measurements has the same shape as the observed gravity but is offset from it by up to 55 mGal at the northern end of the 150 km profile [*Tinto et al.*, 2015]. This offset suggests that some long-wavelength features of the observed gravity field have not been included in the forward model. *Tinto et al.* [2015] estimated the long-wavelength regional gravity field by upward continuing the WGM2012 gravity [*Bonvalot et al.*, 2012] field to 40 km in order to attenuate short-wavelength anomalies resulting from topographic relief and local geologic heterogeneity. Subtracting this regional gravity field from the observed field removed much of the long-wavelength tilt and mismatch between observed and calculated anomalies. This correction was also applied to the gravity data for Newman Bugt (Glacier #71), which is near and runs parallel to Petermann (Figure S4 in the supporting information).

5.2. Other Geological Changes

In southeast Greenland, gravity anomalies tend to increase offshore. In this area, an upward gradient in the gravity begins at ~45 km from the coast. The gravity gradient creates unrealistically shallow modeled bathymetry. This appears to be due to the presence of higher-density flood basalts [e.g., *Hopper et al.*, 2003; *Korenaga et al.*, 2000; *Nielsen*, 1987] in the seaward, eastern portion of these lines. In the results presented here, magnetic data are used to identify changes in geology such as the presence of highly magnetic, dense mafic units along the east coast of Greenland. On many profiles in eastern Greenland, the upward gradient in the gravity anomalies corresponds with distinct change in the character of the magnetic data. We do not model bathymetry seaward of this location (Figure S6 in the supporting information) as this boundary represents the seaward limit of the validity of our inversion.

In northern Greenland, a geological boundary was also revealed by the coincident rise in free-air gravity anomalies and change in magnetic anomalies. This potential field signature corresponds with outcrops of the Paleozoic
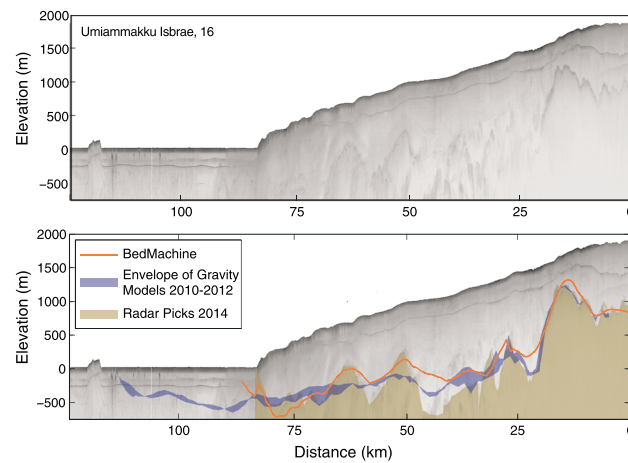
Figure 7. Radar echogram, MCoRDS bed topography, gravity models, and BedMachine [*Morlighem et al.*, 2014] bed topography for Umiammakku Isbrae (Glacier 16). (top) Radar echogram. (bottom) Echogram with the MCoRDS bed from 2014 in brown, the gravity model envelope from 2010 to 2012 models in blue, and the BedMachine grid sampled along the OIB flights in orange.

trough sediments of the Franklinian Basin [*Escher and Pulvertaft*, 1995]. We did not model bathymetry across this boundary as it appears that our homogeneous density assumption does not hold.

5.3. Identification of Sediment

We initially assume that there is no sediment in the fjords, as discussed in section 4.2.2. However, at locations where the bed is known from radar, we can use the gravity results to infer the presence of sediment. When we have a radar-defined grounding line depth and model the bathymetry in the fjord, a positive gravity residual at the grounding line indicates the presence of lower density sediment that we interpret as a moraine. Moraines were identified at Inngia Isbrae (Glacier #17), Kong Oscar (Glacier #44), Tracy (Glacier #64), and Humboldt (Glacier #70).

5.4. Comparison of Bed Models

The gravity models fill in gaps in the radar-derived bed and can also help resolve ambiguities in bed identifications on the radar echograms and thus enhance the interpretation of the radar echograms.

Rink Isbrae (Glacier #15) is an example of a profile where the gravity model indicates a different bed elevation than the radar bed identifications. When we construct a forward model from the known constraints using all ice thickness measurements from radar (Figure 4b), a large gravity residual extends from about 8 to 25 km landward of the grounding line (37–20 km on profile 15.100 in Figure S7 in the supporting information). The radar bed identifications show the bed to deepen by ~1000 m within this interval, but without a corresponding decrease in the gravity anomaly. We eliminated 8 km of radar bed topography measurements that produced this residual (28–20 km on profile 15.100 in Figure S7 in the supporting information) and instead inverted the gravity to model the bed in this portion of the line. The maximum difference between the final gravity-derived bed and the radar identifications in this portion of the line is 610 m. Other examples of where our models suggest bed elevations that are different from radar bed identifications are Daugaard-Jensen (Glacier #92) and Sydbrae (Glacier #101). In these cases, the gravity-derived bathymetry models appear to provide better estimates than the radar bed identifications because we were able to establish our reference density section within the glacial trough, very near the area of the mismatch. The reference density column captures conditions within the trough, leading us to conclude that the mismatch results from misidentification of the radar returns. This differs from Jakobshavn Isbrae, where there was also a large mismatch between the gravity-determined bed and the radar identifications. The radar data along Jakobshavn were sparse, and we were required to define a reference density column inland of the glacial trough, as discussed in the supporting information. As a result, the radar-derived bed at Jakobshavn [*Gogineni et al.*, 2014] appears to be superior to the gravity-determined bed.

Gravity and radar data were collected together until 2012. Since then, MCoRDS has recovered radar-determined bed elevations closer to the grounding lines of several glaciers. In our model for Umiammakku Isbrae (Glacier #16), radar from 2012 imaged only ~27 km of the bed, while gravity filled in the remaining 54 km to the grounding line. The 2014 flight down Umiammakku varied horizontally from the 2010–2012 flight tracks by at most 100 m, and we were able to compare our models with the 2014 radar bed. Figure 7 compares the envelope of our 2010–2012 inversions with the 2014 radar bed identifications. Due to the along-track resolution of the gravity data, the gravity-modeled bed is less detailed than the radar bed but has the same shape and shows the same features in the bed.

Umiammakku Isbrae also offers an opportunity to compare the bed topography obtained from radar gravity and the BedMachine grid [*Morlighem et al.*, 2014]. This grid was generated using ice surface velocity

and the principle of mass conservation to give a smooth interpolation of bed elevation constrained by radar bed determinations. The radar-derived bed shows the greatest range of ice thickness, with maximum depths located at approximately 40 km on the profile. Comparing the other two methods with the radar bed identifications, the BedMachine grid captures the topographic highs but gives significantly shallower depth estimates over topographic lows. The gravity-derived bed produces a filtered version of the radar bed, with lower topography on high points and higher topography on the radar-determined lows (Figure 7).

6. Conclusions

We have used gravity, magnetic, radar, and lidar data collected by Operation IceBridge from 2010 to 2012 to model bathymetry in 54 glacier fjords in Greenland. Although the gravity solution is nonunique, we have arrived at the best solution for each fjord by using knowledge of the physical properties and structure of the Earth. In total, we provide 1950 line kilometers of new bathymetry, which can be further analyzed to explore linkages between glacier mass loss and warming water in the fjords. The models have provided 12 grounding line depths. The gravity models also provide 875 line kilometers of new subice topography in areas where radar from this period did not resolve the bed.

References

Allen, C., C. Leuschen, P. Gogineni, F. Rodriguez-Morales, and J. Paden (2010), *IceBridge MCoRDS L2 Ice Thickness*, NASA National Snow and Ice Data Center Distributed Active Archive Center, Boulder, Colo., doi:10.5067/GDQ0CUCVTE2Q.

Balmino, G., N. Vales, S. Bonvalot, and A. Briais (2012), Spherical harmonic modeling to ultra-high degree of Bouguer and isostatic anomalies, *J. Geod.*, *86*, 499–520, doi:10.1007/s00190-011-0533-4.

Bartholomew, I., P. Nienow, A. Sole, D. Mair, T. Cowton, and M. A. King (2012), Short-term variability in Greenland Ice Sheet morion forced by time-varying meltwater drainage, Implications for the relationship between subglacial drainage system behavior and ice velocity, *J. Geophys. Res.*, *117*, F03002, doi:10.1029/2011JF002220.

Bonvalot, S., G. Balmino, A. Briais, M. Kuhn, A. Petrefitte, and N. Vales (2012), World Gravity Map, Bureau Gravimetrique International (BGI), map GGMW-BGI-CNES-IRD Ed., Paris.

Cochran, J. R., and R. E. Bell (2010), *IceBridge Sander AIRGrav L1B Geolocated Free Air Gravity Anomalies*, NASA National Snow and Ice Data Center Distributed Active Archive Center, Boulder, Colo., doi:10.5067/R1RQ6NRIJV89.

Cochran, J. R., and R. E. Bell (2012), Inversion of IceBridge gravity data for continental shelf bathymetry beneath the Larsen ice shelf, Antarctica, *J. Glaciol.*, *58*, 540–552, doi:10.3189/2012JoG11J033.

Cochran, J. R., S. Elieff, K. J. Tinto, and K. Charles (2011), Ice bridge gravity instrument performance and data assessment, NASA Instrument Summit Rep., 38 pp. [Available at http://www.ldeo.columbia.edu/polar-geophysics-group/publications.]

Cochran, J. R., B. L. Burton, N. Frearson, and K. J. Tinto (2012), *IceBridge Scintrex CS-3 Cesium Magnetometer LIB Geolocated Magnetic Anomalies*, NASA National Snow and Ice Data Center Distributed Active Archive Center, Boulder, Colo., doi:10.5067/Q1APJXOFOMB.

Cochran, J. R., S. S. Jacobs, K. J. Tinto, and R. E. Bell (2014), Bathymetric and oceanic controls on Abbot Ice Shelf thickness and stability, *Cryosphere*, *8*, 877–889, doi:10.5194/tc-8-877-2014.

Dobrin, M. B. (1976), *Introduction to Geophyscial Prospecting*, 3rd ed., 630 pp., McGraw-Hill, New York.

Doyle, S. H., A. Hubbard, A. A. W. Fitzpatrick, D. van As, A. B. Mikkelsen, R. Pettersson, and B. Hubbard (2014), Persistent flow accelerationwithin the interior of the Greenland ice sheet, *Geophys. Res. Lett.*, *41*, 899–905, doi:10.1002/2013GL058933.

Escher, J. C., and T. C. R. Pulvertaft (1995), *Geological nmp of Greenland* 1:2,500,000, Geol. Surv. of Greenland, Copenhagen.

Forste, C., et al. (2008), The GeoForschungsZentrum Potsdam/Groupe de Recherche de Geodesie Spatiale satellite-only and combined gravity field models: Eigen-GL04S1 and Eigen-GL04C, *J. Geod.*, *82*, 331–346, doi:10.1007/s00190-007-0183-8.

Gladish, C., D. M. Holland, A. Rosing-Asvid, J. W. Behrens, and J. Boje (2015), Oceanic boundary conditions for Jakobshavn Glacier. Part I: Variability and renewal of Illulisat Icefjord waters, 2001–2014, *J. Phys. Oceanogr.*, *45*, 3–32, doi:10.1175/JPO-D-14-0044.1.

Gogineni, P., et al. (2014), Bed topography of Jakobshaven Isbrae, Greenland, and Byrd Glacier, Antarctica, *J. Glaciol.*, *60*(223), 813–833, doi:10.3189/2014JoG14J129.

Haxby, W. F., G. D. Karner, J. L. LaBrecque, and J. K. Weissel (1983), Digital images of combined oceanic and continental data sets and their use in tectonic studies, *Eos Trans. AGU*, *64*, 995, doi:10.1029/EO064i052p00995.

Hayford, J. F., and W. Bowie (1912), *The Effect of Topography and Isostatic Compensation upon the Intensity of Gravity*, *Coast and Geodetic Surv. Spec. Publ.*, vol. 10, pp. 132, Gov. Print. Off., Wash.

Heimbach, P., and M. Losch (2012), Adjoint sensitivities of subice shelf melt rates to ocean circulation under the Pine Island Ice Shelf, West Antarctica, *Ann. Glaciol.*, *53*, 59–69, doi:10.3189/2012/AoG60A025.

Henriksen, N., A. K. Higgins, F. Kalsbeek, T. Christopher, and R. Pulvertaft (2009), Greenland from Archaean to Quaternary: Descriptive text to the 1995 geological map of Greenland, 1:2,500,00, *Geol. Soc. Denmark Greenland Bull.*, *18*, 1–126.

Holland, D. M., R. H. Thomas, B. De Young, M. H. Ribergaard, and B. Lyberth (2008), Acceleration of Jakobshavn Isbrae triggered by warm subsurface ocean waters, *Nat. Geosci.*, *1*, 659–664, doi:10.1038/ngeo316.

Hopper, J. R., T. Dahl-Jensen, W. S. Holbrook, H. C. Larsen, D. Lizarralde, J. Korenaga, G. M. Kent, and P. B. Kelemen (2003), Structure of the SE Greenland margin from seismic reflection and refraction data: Implications for a nascent spreading center subsidence and asymmetric crustal accretion during North Atlantic opening, *J. Geophys. Res.*, *108*(B5), 2269, doi:10.1029/2002JB001996.

Johnson, H. L., A. Müenchow, K. K. Falkner, and H. Melling (2011), Ocean circulation and properties in Petermann Fjord, Greenland, *J. Geophys. Res.*, *116*, C01003, doi:10.1029/2010JC006519.

Joughin, I., S. B. Das, M. A. King, B. E. Smith, I. M. Howat, and T. Moon (2008), Seasonal speedup along the western flank of the Greenland Ice Shelf, *Science*, *330*, 781–783, doi:10.1126/science.1153288.

Korenaga, J., W. S. Holbrook, G. M. Kent, P. B. Kelemen, R. S. Detrick, H. C. Larsen, J. R. Hopper, and T. Dahl-Jensen (2000), Crustal structure of the southeast Greenland margin from joint refraction and reflection seismic tomography, *J. Geophys. Res.*, *105*, 21,591–521,614, doi:10.1029/2000JB900188.

Krabill, W. (2014), *IceBridge ATM L2 Icessn Elevation, Slope, and Roughness, Version 2*. NASA National Snow and Ice Data Center Distributed Active Archive Center, Boulder, Colo., doi:10.5067/FCCzIIFRPZ30.

Krabill, W., R. Thomas, K. C. Jezek, K. Kuivinen, and S. Manizade (1995), Greenland ice sheet thickness changes measured by laser altimetry, *Geophys. Res. Lett.*, *22*, 2341–2344, doi:10.1029/95GL02069.

Leliak, P. (1961), Identification and evaluation of magneticfield sources of magnetic airborne detector equiped aircraft, *IRE Trans. Aerosp. Navig. Electron.*, *8*, 95–105, doi:10.1109/TANE3.1961.4201799.

MacGregor, J. A., M. A. Fahnestock, G. A. Catania, J. D. Paden, S. P. Gogineni, S. K. Young, S. C. Rybarski, A. N. Mabrey, B. M. Wagman, and M. Morlighem (2015), Radiaostratigraphy and age structure of the Greenland Ice Sheet, *J. Geophys. Res. Earth Surf.*, *120*, 212–241, doi:10.1002/2014JF003215.

Martin, C. F., W. B. Krabill, S. S. Manizade, R. L. Russel, J. G. Sonntag, R. N. Swift, and J. K. Yungel (2012), Airborne topographic mapper calibration procedures and accuracy assessment, *NASA Tech. Rep. NASA/TM-2012-215891*, 32 pp., Greenbelt, Md.

Meirbachtol, T., J. Harper, and N. Humphry (2013), Basal drainage system response to increasing surface melt on the Greenland Ice Sheet, *Science*, *341*, 777–779, doi:10.1126/science.1235905.

Moon, T., I. Joughin, B. Smith, and I. M. Howat (2012), 21st-century evolution of Greenland outlet glacier velocities, *Science*, *336*, 576–578.

Moritz, H. (2000), Geodetic Reference System 1980, *J. Geod.*, *74*, 128–133.

Morlighem, M., E. Rignot, J. Mouginot, H. Seroussi, and E. Larour (2014), Deeply incised submarine glacial valleys beneath the Greenland Ice Sheet, *Nat. Geosci.*, *7*, 418–422, doi:10.1038/ngeo2167.

Mortensen, J., K. Lennert, J. Bendtsen, and S. Rysgaard (2011), Heat sources for glacial melt in a sub-Arctic fjord (Godthabsfjord) in contact with the Greenland Ice Sheet, *J. Geophys. Res.*, *116*, C01013, doi:10.1029/2010JC006528.

Mortensen, J., J. Bendtsen, K. Lennert, and S. Rysgaard (2014), Seasonal variability of the circulation system in in a wet Greenland tidewater outlet glacier fjord, Godthabsfjord (64°N), *J. Geophys. Res. Earth Surf.*, *119*, 2591–2603, doi:10.1002/2014JF003267.

Muto, A., S. Anandakrishnan, and R. B. Alley (2013), Subglacial bathymetry and sediment layer distribution beneath the Pine Island Glacier ice shelf, West Antarctica, modeled using aerogravity and autonomous underwater vehicle data, *Ann. Glaciol.*, *54*, 27–32, doi:10.3189/2013AoG64A110.

Myers, P. G., and M. H. Ribergaard (2013), Warming of the polar water layer in Disko Bay and potential impact on Jalobshavn Isbrae, *J. Phys. Oceanogr.*, *43*, 2629–2640, doi:10.1175/JPO-D-12-051.1.

Nick, F. M., A. Vieli, I. M. Howat, and I. Joughin (2009), Large-scale changes in Greenland outlet glacier dynamics triggered at the terminus, *Nat. Geosci.*, *2*, 110–114, doi:10.1038/NGEO394.

Nielsen, T. F. D. (1987), Tertiary alkaline magmatism in East Greenland: A review, in *Alkaline Igneous Rocks*, *Spec. Publ.*, vol. 30, edited by J. G. Fitton and B. G. J. Upton, pp. 489–515, Geol. Soc., London.

Noriega, G. (2011), Performance measures in aeromagnetic compensation, *Leading Edge*, *30*, 1122–1127, doi:10.1190/1.3657070.

Padman, L., et al. (2012), Oceanic controls on the mass balance of Wilkins Ice Shelf, Antarctica, *J. Geophys. Res.*, *117*, C01010, doi:10.1029/2011JC007301.

Porter, D., K. J. Tinto, A. Boghosian, J. R. Cochran, R. E. Bell, S. Manizade, and J. Sonntag (2014), Bathymetric control of tidewater glacier mass loss in northwest Greenland, *Earth Planet. Sci. Lett.*, *401*, 40–46, doi:10.1016/j.epsl2014.05058.

Rignot, E., and P. Kanagaratnam (2006), Changes in the velocity structure of the Greenland Ice Sheet, *Science*, *311*, 986–990, doi:10.1126/science.1121381.

Rignot, E., and J. Mouginot (2012), Ice flow in Greenland for the international polar year 2008–2009, *Geophys. Res. Lett.*, *39*, L11501, doi:10.1029/2012GL051634.

Rignot, E., I. Fenty, D. Menenlis, and Y. Xu (2012), Spreading of warm waters around Greenland as a possible cause for glacier acceleration, *Ann. Glaciol.*, *53*, 257–266, doi:10.3189/2012AoG60A136.

Sander, S., M. Argyle, S. Elieff, S. Ferguson, V. Lavoie, and L. Sander (2004), The AIRGrav aiborne gravity system, in *Airborne Gravity 2004 - Australian Society of Exploration Geophysicists Workshop*, edited by R. Lane, pp. 49–53, Geoscience Australia, Sydney, Australia. [Available at http://sgl.com/technicalpapers/AIRGrav_airborne_grav_sys.pdf.]

Sandwell, D. T., R. D. Muller, W. H. F. Smith, E. Garcia, and R. Francis (2014), New global marine gravity model from CryoSat-2 and Jason-1 reveals buried tectonic structure, *Science*, *346*(6201), 65–67, doi:10.1126/science.1258213.

Schodlok, M., D. Menemenlis, E. Rignot, and M. Studinger (2012), Sensitivity of the ice-shelf/ocean system to the sub ice-ishelf cavity shape measured by NASA IceBridge in Pine Island Glacier, West Antarctica, *Ann. Glaciol.*, *53*, 156–162, doi:10.3189/2012A0G60A073.

Schumann, K., D. Volker, and W. R. Weinrebe (2012), Acoustic mapping of the Illulisat Ice Fjord mout, West Greenland, *Quat. Sci. Rev.*, *40*, 78–88, doi:10.1016/j.quascirev.2012.02.016.

Seale, A., P. Christoffersen, R. I. Mugford, and M. O'Leary (2011), Ocean forcing of the Greenland Ice Sheet: Calving fronts and patterns of retreat identified by automatic satellite monitoring of eastern outlet glaciers, *J. Geophys. Res.*, *116*, F03013, doi:10.1029/2010JF001847.

Shepherd, A., et al. (2012), A reconciled estimate of ice-sheet mass balance, *Science*, *338*, 1183–1189, doi:10.1126/science.1228102.

Smith, D. V., Phillips, J. D., and S. R. Hutton, (2014), Active tensor magnetic gradiometer system final report for Project MM–1514, *U.S. Geol. Surv. Open-File Rep. 2013–1228*, 39 pp., doi:10.3133/ofr20131228.

Smith, W. H. F., and D. T. Sandwell (1997), Global sea floor topography from satellite altimetry and ship depth soundings, *Science*, *277*, 1956–1962.

Straneo, F., D. A. Sutherland, D. Holland, C. Gladish, G. S. Hamilton, H. L. Johnson, E. Rignot, Y. Xu, and M. Koppes (2012), Chracteristics of ocean water reaching Greenland's glaciers, *Ann. Glaciol.*, *53*, 202–210, doi:10.3189/2012AoG60A059.

Studinger, M., R. E. Bell, and N. Frearson (2008), Comparison of AIRGrav and GT-1A airborne gravimeters for research applications, *Geophysics*, *73*, 151–161.

Stygebrandt, A. (2012), Hydrodynamics and circulation of fjords, in *Encyclodepia of Lakes and Reservoirs*, edited by L. Bengtsson, R. W. Herschy, and R. W. Fairbridge, pp. 327–344, Springer, Netherlands.

Syvitski, J. P., and J. Shaw (1995), Sedimentology and geomorphology of fjords, in *Geomorphology and Sedimentology of Estuaries*, *Dev. Sedimentol.*, vol. 53, edited by G. M. E. Perillo, pp. 113–178, Elsevier Science, Amsterdam, Netherlands.

Talwani, M., J. L. Worzel, and M. Landisman (1959), Rapid gravity computations for two-dimensional bodies with application to the Mendocino submarine fracture zone, *J. Geophys. Res.*, *64*, 49–59, doi:10.1029/JZ064i001p00049.

Telford, W. M., L. P. Geldart, and R. E. Sheriff (1990), *Applied Geophysics*, 2nd ed., 770 pp., Cambridge Univ. Press, Cambridge.

Tinto, K. J., and R. E. Bell (2011), Progressive unpinning of Thwaites Glacier from newly identified offshore ridge: Constraints from aerogravity, *Geophys. Res. Lett.*, *38*, L20503, doi:10.1029/2011GL049026.

Tinto, K. J., R. E. Bell, J. R. Cochran, and A. Munchow (2015), Bathymetry in Petermann Fjord from Operation IceBridge aerogravity, *Earth Planet. Sci. Lett.*, *422*, 58–66, doi:10.1016/.j.epsl.2015.04009.

Zwally, H. J., W. Abdalati, T. Herring, K. Larson, J. L. Saba, and K. Steffen (2002), Surface melt-induced acceleration of Greenland ice-sheet flow, *Science*, *297*, 218–222, doi:10.1126/science.1072708.